N. A. Tsyganenko and V. A. Andreeva Date: 10/10/2015

Department of the Earth's Physics, Saint-Petersburg State University, Saint-Petersburg, Russia.

Forecasting models of the magnetosphere driven by optimal solar-wind coupling functions.

This article presents a concise synopsis of a new empirical model of the Earth's magnetosphere based on satellite data and driven by input parameters inferred from observations in the upstream solar wind. A systematic description of the model's structure and underlying data can be found in a recent paper [*Tsyganenko and Andreeva, J. Geophys. Res.,* v.**120**, 2015, in press, referred to below as *TA15*]. The purpose of this document is two-fold. First, we briefly describe basic features of the new model, including its recent upgrade (made after the acceptance of *TA15* and not covered in that publication). Second, an alternative version of the model is also discussed, based on another interplanetary driver function.

1. Spacecraft data.

The modeling data set was created on the basis of magnetic field observations made during the period 1995–2013 onboard Geotail, Polar, Cluster, and five Themis satellites. The 'grand' data set included in total 3,862,837 five-minute average data records. To exclude strong storms and intervals of extremely unusual magnetospheric and interplanetary conditions, the model was actually fitted to a somewhat smaller set with 3,372,032 records, in which only those data were retained that satisfied certain limitations, as listed in the following Table. Spatial distribution of the data is shown in Fig.1 below.

	Lower limit	Upper limit
Geocentric distance R, RE	3	60
IMF Bx (GSM), nT	–10	+10
IMF By (GSM) , nT	–10	+10
IMF Bz (GSM) , nT	–10	+10
Solar wind ram pressure, nPa	0.4	6.0
Solar wind speed, km/s	250	800
N-index (Eq.(1) below)	0.0	2.0
B-index (Eq.(2) below)	0.0	2.0
Sym-H	–100	40

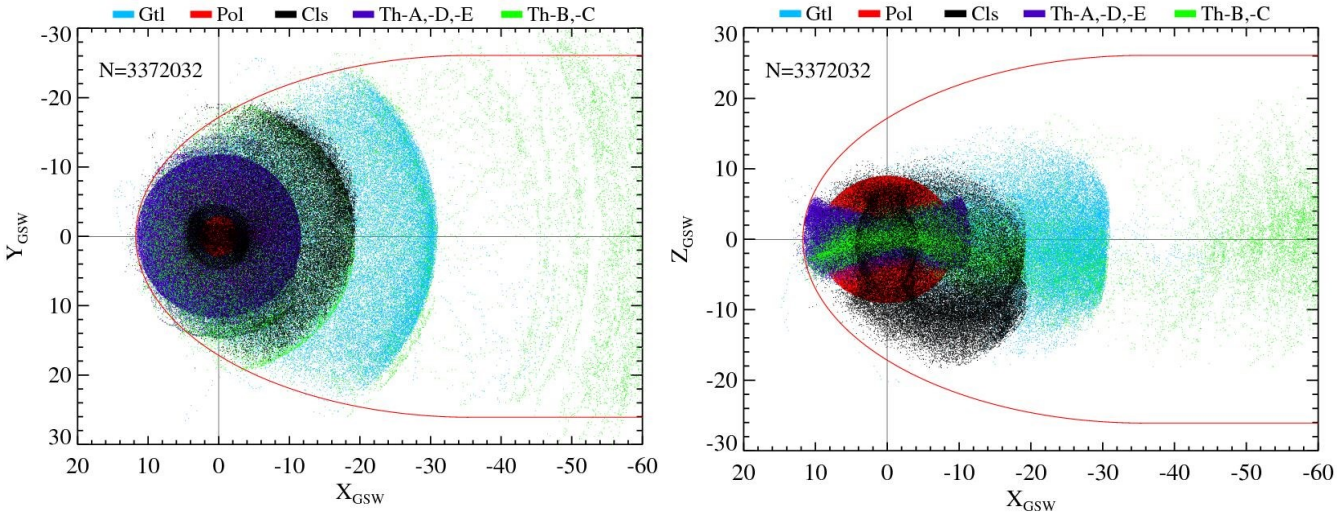

Fig.1. Spatial distribution of spacecraft data records, projected onto XY and XZ planes.

2. Interplanetary coupling functions.

Two versions of the model have been developed under this project. The first version included as a driving input quantity a solar wind coupling function, suggested by *Newell et al*. [2007] as an optimal parameter best correlated with 10 magnetospheric state variables, including both its inner low-latitude characteristics (Dst, geosynchronous field inclination, isotropy boundary b2i) and high-latitude parameters (polar cap size, cusp latitude, AE/AL indices, auroral power). We used a normalized Newell's function (called henceforth the '$\mathcal{N}$-index'), defined as

$$\mathcal{N} = 10^{-4} V^{\frac{4}{3}} B_T^{\frac{2}{3}} \sin^{\frac{8}{3}} \frac{\theta_c}{2} = 0.86 \left[\frac{V}{400}\right]^{\frac{4}{3}} \left[\frac{B_T}{5}\right]^{\frac{2}{3}} \sin^{\frac{8}{3}} \frac{\theta_c}{2} \tag{1}$$

and typically varying within a range between 0 and 2. Here V, B_T, and θ_c are the solar wind speed (in km/s), transverse component of the IMF (nT), and its clock angle, respectively.

In the second version of the model we used another interplanetary index, based on the coupling function by *Boynton et al.* [2011], derived as an optimal predictor for the Dst-index. The corresponding normalized driving function used in this study (termed henceforth as the '$\mathcal{B}$-index') reads

$$\mathcal{B} = \left[\frac{n_p}{5}\right]^{\frac{1}{2}} \left[\frac{V}{400}\right]^{\frac{5}{2}} \frac{B_T}{5} \sin^6 \frac{\theta_c}{2} \tag{2}$$

where n_p is the solar wind proton density in cm^{-3}. Note that, unlike in the original works by *Newell et al.* and *Boynton et al.* (based on hourly averages), we calculated both the $\mathcal{N}$- and $\mathcal{B}$-indices using 5-min average values of the interplanetary parameters from the OMNI database. For any given time moment, $\mathcal{N}$ and $\mathcal{B}$ values were calculated as arithmetic mean of 7 five-minute averages, including that for the present moment and 6 records covering the immediately preceding 30-minute interval.

3. Modular structure.

The external part of the magnetospheric magnetic field (due to only the extraterrestrial sources) is represented as a sum of six separate terms (modules):

$$\mathbf{B}_{\mathrm{E}} = \mathbf{B}_{\mathrm{CF}} + \mathbf{B}_{\mathrm{SRC}} + \mathbf{B}_{\mathrm{PRC}} + \mathbf{B}_{\mathrm{TC}} + \mathbf{B}_{\mathrm{R1\ FAC}} + \kappa \mathbf{B}_{\perp \mathrm{IMF}} \tag{3}$$

which represent contributions, respectively, from the Chapman-Ferraro current on the magnetopause (the dipole shielding field), symmetric (SRC) and partial (PRC) ring current (including the associated Region 2 field-aligned currents, R2 FACs), tail current (TC), Region 1 FACs, and a penetrating part of the transverse component of the IMF. In a more explicit setting, equation (3) takes on the form

$$\begin{aligned} \mathbf{B}_{\mathrm{E}} = \mathbf{B}_{\mathrm{CF}} + \left(a_{\mathrm{src}}^{(0)} + a_{\mathrm{src}}^{(1)} \Psi^2\right) \cdot \mathbf{b}_{\mathrm{src}} + \left(a_{\mathrm{prc}}^{(0)} + a_{\mathrm{prc}}^{(1)} \Psi^2\right) \cdot \mathbf{b}_{\mathrm{prc}} + \left(a_{\mathrm{tc}}^{(0)} + a_{\mathrm{tc}}^{(1)} \Psi^2\right) F_p \cdot \mathbf{b}_{\mathrm{tc}} \\ + \left(a_{\mathrm{r1r}}^{(0)} + a_{\mathrm{r1r}}^{(1)} \Psi^2\right) \cdot \mathbf{b}_{\mathrm{r1r}} + a_{\mathrm{r1a}} \Psi \cdot \mathbf{b}_{\mathrm{r1a}} + \kappa \mathbf{B}_{\perp \mathrm{IMF}} \end{aligned} \tag{4}$$

The dipole shielding field $\mathbf{B}_{\mathrm{CF}}$ is uniquely defined by the shape and size of the model magnetopause (a simplified version of *Lin et al*. [2010] model), driven by the solar wind pressure P_{dyn}, IMF B_z, and the dipole tilt angle Ψ. The next four terms in (4) correspond to the vectors $\mathbf{B}_{\mathrm{SRC}}$, $\mathbf{B}_{\mathrm{PRC}}$, $\mathbf{B}_{\mathrm{TC}}$, and $\mathbf{B}_{\mathrm{R1\ FAC}}$ in (3), each represented as a product of a magnitude coefficient and a normalized 'basis' vector field of the individual source $\mathbf{b}_{...}$. The coefficients, in turn, are split into binomials of the form $a^{(0)} + a^{(1)}\Psi^2$, to

take into account the modulation of magnetospheric currents by the geodipole tilt angle Ψ. The magnetotail field term also includes the factor $F_p = [P_{\rm dyn}/\langle P_{\rm dyn}\rangle]^{\zeta}$ which accounts for the modulation of the tail current by the solar wind pressure. The terms containing the basis vectors $\mathbf{b}_{\rm r1r}$ and $\mathbf{b}_{\rm r1a}$ represent two submodules of the R1 FAC system: the regular symmetric submodule (r1r) with equal downward (upward) currents in both hemispheres at dawn (dusk), and the antisymmetric submodule (r1a) with opposite polarities of FACs in the northern and southern hemispheres. The antisymmetric term is an odd (linear) function of Ψ, included to take into account the possibility of seasonal/diurnal asymmetry of the FACs due to (i) the difference in the ionospheric conductivity between the summer and winter hemispheres and (ii) the global tilt-induced asymmetry of the R1 FAC generator in the magnetospheric boundary layer and in the magnetosheath. Each basis vector field $\mathbf{b}_{...}$ in (4) includes its individual shielding field, which ensures that the total field remains confined within the magnetopause for any combination of values of the magnitude coefficients and for any dipole tilt angle.

As represented by Eq.(4), the model includes 10 unknown coefficients and 13 nonlinear parameters, defining the geometry of individual field sources and their response to the solar wind pressure via the scaling and magnitude factors. The solar wind driving of the magnetosphere due to the IMF-related processes was introduced into the model by expanding each of the 23 model parameters into quadratic trinomials of the $\mathcal{N}$- and $\mathcal{B}$-indices and subsequent fitting of their coefficients to the data, as described below in more detail.

4. Parameterizing the model with $\mathcal{N}$- and $\mathcal{B}$-indices.

A common problem with the solar wind/IMF data is a dramatic disparity in the density of quiet- and storm-time data. Fig.2 shows histograms of the occurrence frequency M of both $\mathcal{N}$- and $\mathcal{B}$-indices, based on the entire set of data used in the modeling.

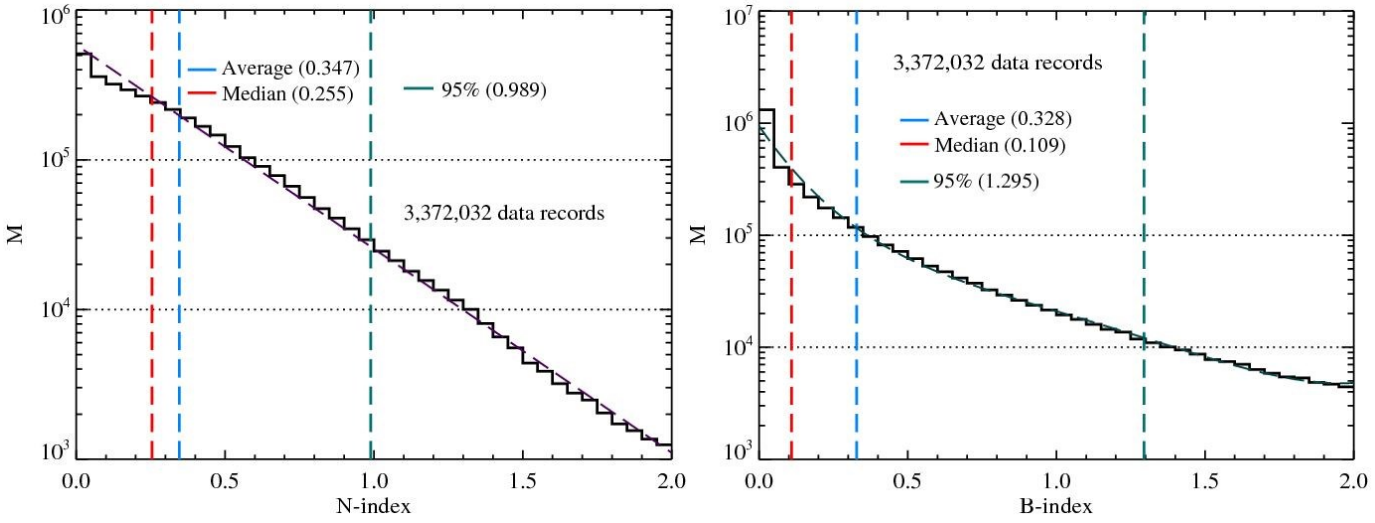

Fig.2. Histograms of the $\mathcal{N}$- and $\mathcal{B}$-index occurrence frequency (left and right panels, resp.), obtained on the basis of entire modeling dataset. Analytical fits are shown by dashed lines in both plots.

The approximately linear decrease of $\log_{10}$M in the case of the $\mathcal{N}$-index (left panel) and an even faster drop-off in the $\mathcal{B}$-index histogram indicate an exponential reduction of the data density at the high end of the $\mathcal{N}/\mathcal{B}$ range. Indiscriminate use of such non-uniform data would imply a severe disbalance between quiet and storm-time data, which might result in strongly biased values of the model parameters. In

the *TA15* version of the model, that problem was mitigated by a selective thinning of the data, which partially equalized their density at the low end of the $\mathcal{N}$-index range and, at the same time, resulted in a ~6-7-fold shrinking of the data set (down to 545,709 data records). In the latest effort, a different method was employed, based on the entire dataset with weighted records. Somewhat surprisingly, no significant changes from the original version were found in the fitting results, as described in the next section.

5. Fitting the model to the data.

As in our previous modeling projects, we used an iterative fitting algorithm, based on a downhill simplex search in the space of nonlinear parameters, in which the magnitude coefficients were updated at each step using the singular value decomposition method. The fitting procedure included two basic steps. First of all, the thinned (equalized) subset of the grand data set with the 545,709 records was further divided into 11 smaller subsets, corresponding to a sequence of 11 successive intervals of the $\mathcal{N}$-index covering the interval $0 \le \mathcal{N} \le 1.5$. Data from each of the 11 bins (typically amounting from ~40,000 to ~100,000 data records) were then used to find best-fit values of the 23 model parameters. As a result, sequences of 11 best-fit values were obtained for each of the 23 parameters, representing their variation over the wide range of $\mathcal{N}$. Each of the sequences was then approximated by a quadratic trinomial of $\mathcal{N}$, which resulted in a set of 23x3=69 coefficients. Those coefficients represented, in fact, the final *TA15* version of the model.

In the most recent upgrade of the model (not covered in *TA15*), instead of the above described selective thinning of the data with their subsequent binning, we implemented a completely different approach, in which (1) the model parameters were assumed from the outset in the form of quadratic trinomials and, (2) the entire original dataset was used to derive the model parameters. The data disparity problem was solved in this case by assigning to each record a weight, inversely proportional to the data density as defined from the above histograms. To that end, the $\mathcal{N}$- and $\mathcal{B}$- distributions of data presented in Fig.2 were approximated by the following best-fit exponential forms (dashed lines in the Fig.2 plots)

$$M(\mathcal{N}) = 10^{5.77-1.36\mathcal{N}} \qquad \text{for } \mathcal{N}\text{-index} \qquad (5)$$

$$M(\mathcal{B}) = 10^{5.97-3.87\mathcal{B}+4.08\mathcal{B}^2-2.36\mathcal{B}^3+0.50\mathcal{B}^4} \qquad \text{for } \mathcal{B}\text{-index} \qquad (6)$$

and each record in the grand modeling set was tagged with the corresponding weights, calculated as inverse of the occurrence frequency: $W_k = M_k^{-1}$. In that approach, the corresponding target functions to be minimized have the form

$$\sigma = \sqrt{\sum_{k=1}^{N} \left\{ W_k \cdot \left[\mathbf{B}_{\text{model}}(\mathbf{r}_k) - \mathbf{B}_k \right]^2 \right\} \Big/ \sum_{k=1}^{N} W_k} \ . \qquad (7)$$

Note that while using the entire dataset instead of the thinned one is conceptually more consistent, it is more complicated technically, (1) due to the 3-fold increase in the number of model parameters (from 23 to the total of 69, including 39 nonlinear parameters) and (2) owing to much larger (by the factor 6–7) data set. The first hurdle was overcome by using the *TA15* nonlinear parameter values as starting guess values, which prevented the minimization algorithm to miss the global minimum. The much larger size of the data set inevitably resulted in a much longer computation time; that problem was mitigated by running the code on 8 processors in the MPI environment.

6. Results: $\mathcal{N}$- and $\mathcal{B}$-driven versions of the model.

In general, the best-fit parameters obtained for the upgraded version of the model with the above described modifications were found to be fairly close to those in the original one, based on binning the data into $\mathcal{N}$-index intervals and presented in the *TA15* publication. In the upgraded $\mathcal{N}$-driven model fitted to the entire grand dataset, the most significant difference from the earlier *TA15* version is in the behavior of the principal field source magnitudes at the high end of the $\mathcal{N}$-index range. Figure 3 illustrates the upgrading results in a set of panels, similar in their format to Figs.12–14 of *TA15*, but with two more curves added, showing the variation of the corresponding parameters with $\mathcal{N}$ (red) and $\mathcal{B}$ (green) indices, obtained in the global fitting of the model to the full set of data. For comparison, the original parabolic approximations to the values derived for individual data bins (black dots) are also shown (blue traces).

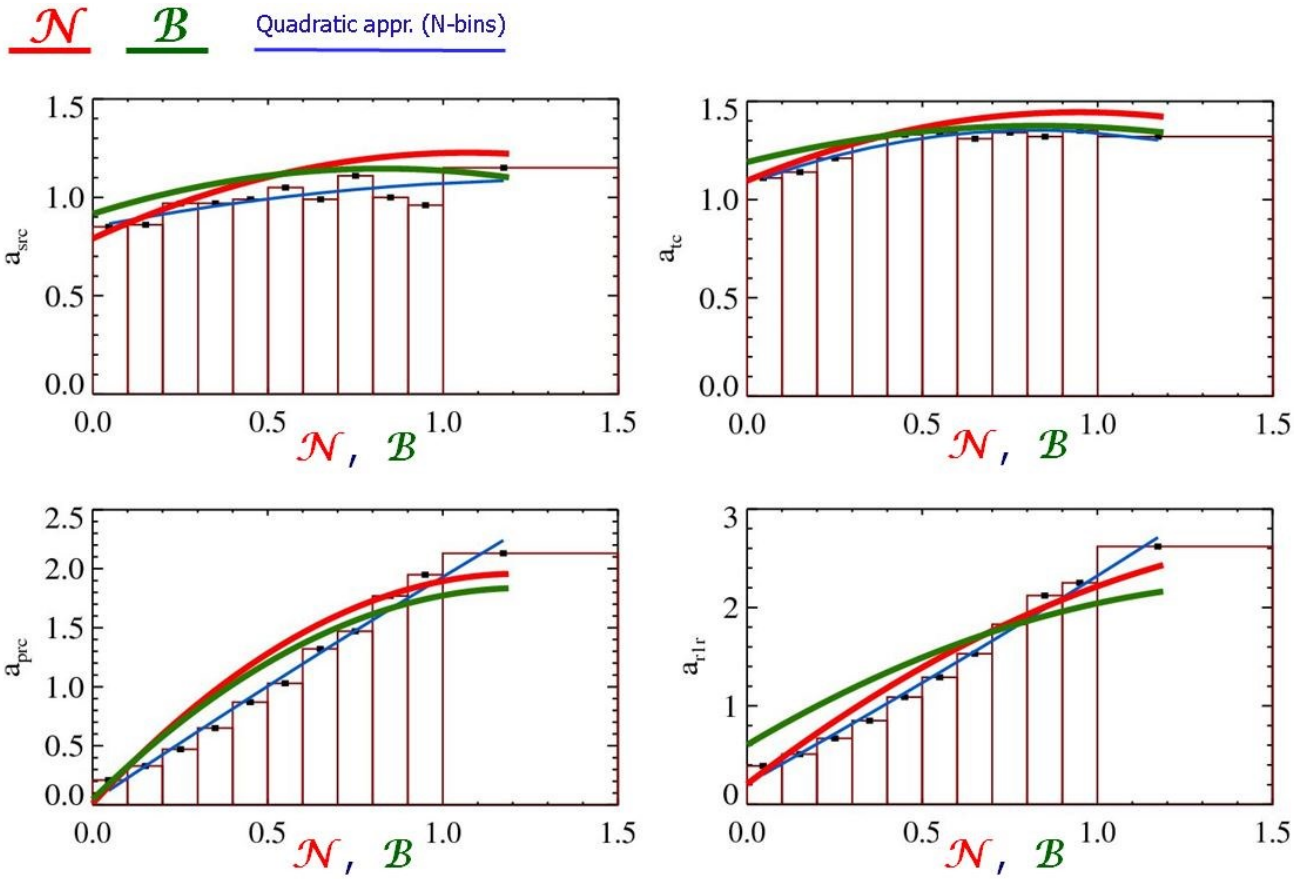

Fig.3. Magnitudes of the SRC (top left), TC (top right), PRC (bottom left), and R1 FAC (regular mode, bottom right), as functions of the $\mathcal{N}$- (red) and $\mathcal{B}$-indices. The original *TA15* results (used as starting values in the global fitting) are also shown (blue).

As can be seen in the plots, in the upgraded version of the model the magnitudes of all the principal field sources grow faster at the low end of the $\mathcal{N}$- and $\mathcal{B}$- range, but reveal a tendency for saturation toward the high end. Note also that switching to the $\mathcal{B}$-index from $\mathcal{N}$ does not result in any significant change of the model field for the same values of those parameters.

The next set of plots in Figure 4 illustrates the effect of the dipole tilt angle on the magnitude of the field sources. Note the negative polarity of all the coefficients in virtually the entire range of both $\mathcal{N}$- and $\mathcal{B}$-index, which manifests the general decrease of the total current in all magnetospheric field sources with growing tilt angle of the Earth's dipole axis.

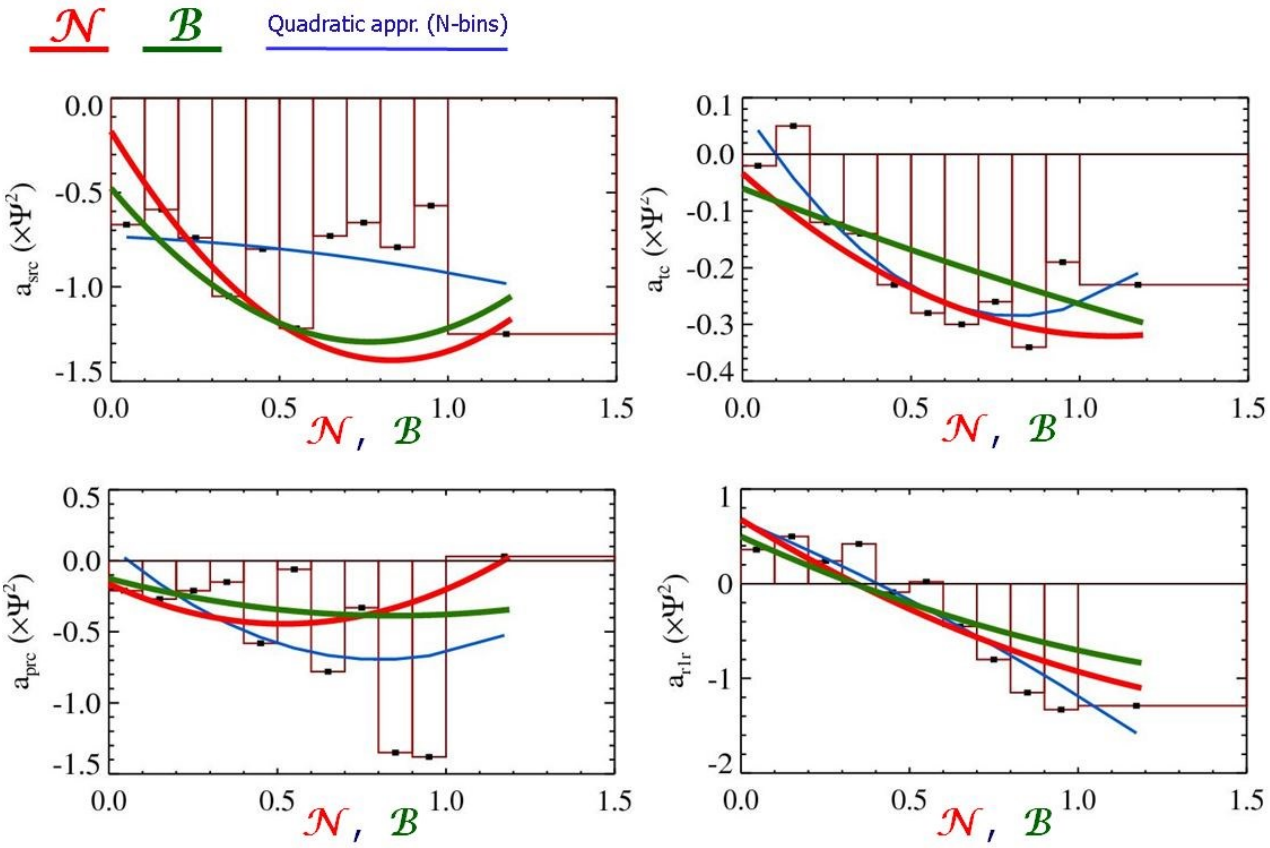

Fig.4. Magnitudes of the tilt-dependent terms in (4) vs. $\mathcal{N}$ and $\mathcal{B}$. The plot illustrates their overall decrease with growing dipole tilt angle and variation of that effect with $\mathcal{N}$- and $\mathcal{B}$-indices.

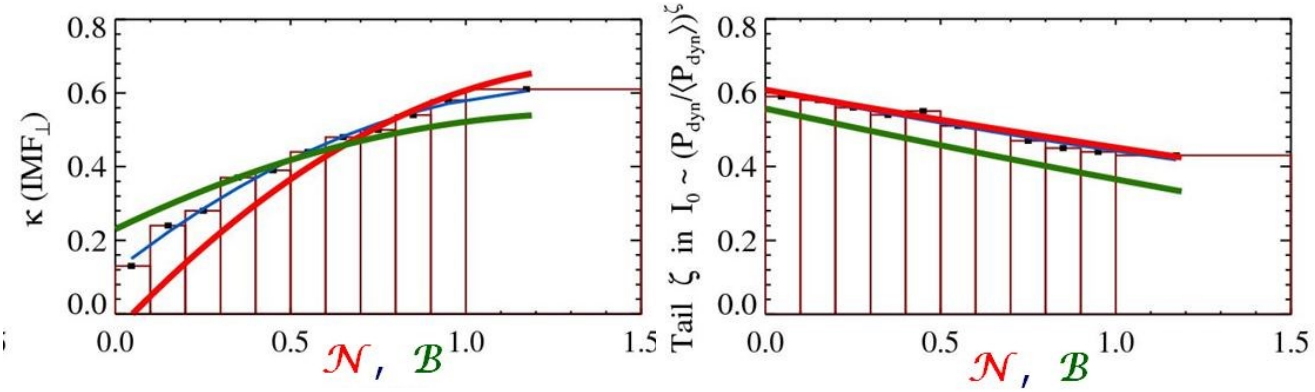

Fig.5. Left: the IMF penetration coefficient and (right) the power exponent ζ in the factor defining the tail current response to the solar wind ram pressure, as functions of the $\mathcal{N}$- and $\mathcal{B}$-indices.

Finally, the pair of plots in Figure 5 displays the $\mathcal{N}$- and $\mathcal{B}$-dependence of the IMF penetration coefficient (left panel) and of the power exponent ζ quantifying the tail current sensitivity to the ram pressure of the solar wind. The only notable difference can be seen between the $\mathcal{N}$- and $\mathcal{B}$-plots for the IMF pe-

netration in the left panel: the former one rises steeper with growing $\mathcal{N}$, and the penetration effect virtually disappears at $\mathcal{N}$~0, while the dependence of κ on $\mathcal{B}$ is generally weaker and the penetration is yet tangible (κ≈0.25) at $\mathcal{B}$=0.

The field line plots, FAC diagrams, and equatorial distributions of the field depression/compression obtained with the upgraded version, are quite similar to those in the original model and hence not reproduced here (see Figs.16–18 of *TA15*). As concerns the model's fidelity in representing the observed magnetic field, one might expect some difference between the original and upgraded versions, in view of a significantly different way of handling the data and the model parameter derivation. However, and again contrary to expectations, the difference was found to be virtually negligible. To illustrate this, Figure 6 presents scatterplots of the model $\{B_x, B_y, B_z\}$ (with the IGRF contribution subtracted) against the corresponding observed components. The plots are analogous to Figure 15 of *TA15*, except how the data are presented: (a) the axes orientation is swapped, so that the model/observed **B** components are now plotted along the horizontal/vertical axes, and (b) a much more informative method is employed to visualize the data scatter around the diagonal. Namely, instead of directly plotting the cloud of dots each representing an individual data record (as was done in *TA15*), we divide the plotting area into square bins 1nT x 1nT and color them according to the number of points falling in each bin. The resulting distributions (Fig.6) reveal a central core (red/yellow) stretched along the diagonal and containing most part of data, enveloped within a much sparser 'penumbra' distribution, with several interesting details.

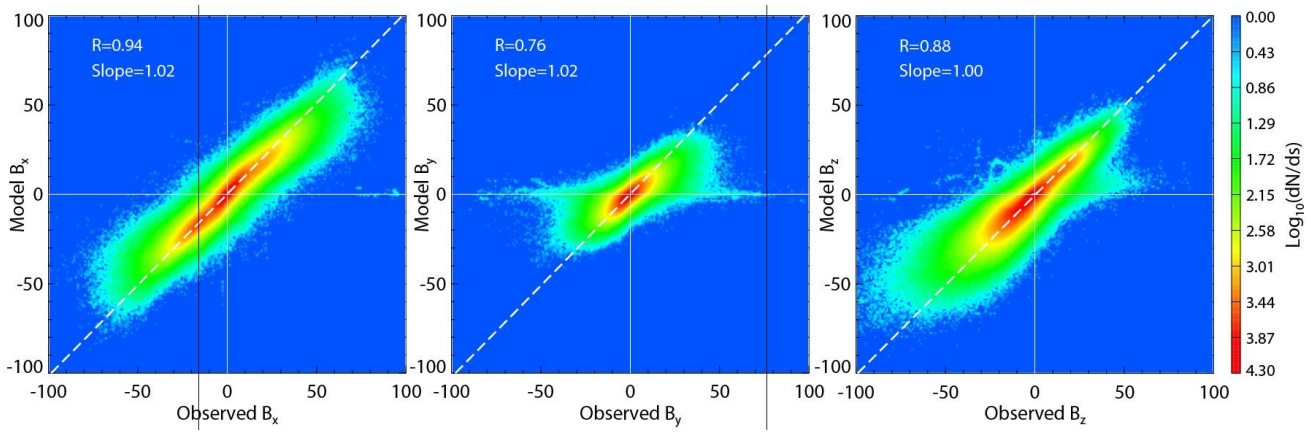

Fig.6. Scatterplots of the model vs observed components of the external part of magnetospheric magnetic field, based on the entire set of 3,372,032 data records. The plots correspond to the $\mathcal{N}$-driven version of the model.

First, the green penumbra in the B_x panel is slightly tilted clockwise with respect to the main diagonal, most likely due to understretched model field for strongly disturbed periods, which is also reflected in an upward shift of the left part of B_z distribution (right panel) for B_z <-50nT. Second, there is an extended and narrow horizontal streak in the B_y distribution (already discussed earlier, e.g., [*Tsyganenko*, 2002, 2009]), revealing the model's inability to replicate the effect of Region 0 FACs on the dayside, induced by the azimuthal component of the IMF. Third, a conspicuous lateral bulge in the B_z distribution with observed B_z ~ 50 and much smaller positive model B_z reveals the effect of the polar cusp diamagnetism [*Tsyganenko and Russell*, 1999; *Tsyganenko,* 2009], which results in a positive B_z disturbance in both northern and southern cusps, not reproduced by the model.

Concerning the correlation and slope differences between the *TA15* version (based on the $\mathcal{N}$-index and thinned/binned dataset) and the present upgraded $\mathcal{N}$-model (fitted to the full dataset), the only changes are (a) in the B_y correlation coefficient which slightly decreased from R=0.77 in *TA15* to R=0.76, and (b) in a slightly improved B_z slope: from 1.01 in TA15 to 1.00 in the upgraded full-set version. It is also worth comparing the performance in these terms of the $\mathcal{N}$-based upgraded version with that of the $\mathcal{B}$-version. The scatterplot for the $\mathcal{B}$-version is virtually indistinguishable from that based on the $\mathcal{N}$-index and hence not reproduced here. Regarding the correlation and slopes, the $\mathcal{B}$-based version shows an improvement in the B_x slope (a perfect 1.00 against 1.01 in the case of $\mathcal{N}$-version), but worse results for B_y (correlation and slope equal to 0.75 and 1.03, against 0.76 and 1.02 in the $\mathcal{N}$-case, respectively).

7. Fortran source codes and yearly input parameter data files.

Two Fortran source codes are provided, named TA_2015_N.for and TA_2015_B.for and corresponding to the $\mathcal{N}$- and $\mathcal{B}$- based versions of the model. The input parameters are explained in the opening comment lines of both files. To facilitate using the model for specific time intervals in the past, a set of yearly data files has been created, based on five-minute average interplanetary parameters downloaded from the OMNI website (http://omniweb.gsfc.nasa.gov/form/omni_min.html). The files can be accessed from the webpage containing this document; below is a list of the data in each record along with their format.

IYEAR	i4	4-digit year
IDAY	i4	Day of year (IDAY=1 is January 1)
IHOUR	i3	UT hour (0 – 23)
MIN	i3	UT minute (0 – 59)
<Bx IMF>	f8.2	nT, in GSW* coordinates, average over 30-min trailing interval
<By IMF>	f8.2	nT, in GSW* coordinates, average over 30-min trailing interval
<Bz IMF>	f8.2	nT, in GSW* coordinates, average over 30-min trailing interval
Vx	f8.1	solar wind Vx in GSE coordinates, km/s
Vy	f8.1	solar wind Vy in GSE coordinates, km/s
Vz	f8.1	solar wind Vz in GSE coordinates, km/s
Np	f7.2	solar wind proton density, cc^{-1}
T	f9.0	solar wind proton temperature, degs K
Sym-H	f7.1	Sym-H index
IMF flag	i5	equals 1 (2) for actually measured (linearly interpolated) IMF
SW flag	i5	equals 1 (2) for actually measured (linearly interpolated) solar wind parameters
Tilt	f8.4	geodipole tilt angle (radians!) in GSW coordinate system
Pdyn	f7.2	solar wind flow ram pressure, nPa
$\mathcal{N}$-index	f8.4	as defined by Eq.(1) above, average over 30-min trailing interval
$\mathcal{B}$-index	f8.4	as defined by Eq.(2) above, average over 30-min trailing interval

*) GSW coordinate system differs from the standard GSM in that its X axis is antiparallel to the solar wind flow direction, rather than the Earth-Sun line. Transformations from GSM to GSW and back can be done by means of

the GEOPACK-2008 package, available from this website.

8. Caveats and limitations of the model.

As already noted in Section 1, both $\mathcal{N}$- and $\mathcal{B}$-based versions of the model were fitted to a filtered data set, from which all records were removed that did not meet the limits imposed on the concurrent interplanetary parameters, Sym-H index, and geocentric distance of the observing spacecraft, listed in the Table in Section 1. For that reason, setting the model input parameters at values outside those limits may result in largely biased and meaningless output field vectors. It should also be realized that the model is inherently statistical and based on static field sources. Therefore it cannot faithfully reproduce transient dynamic events, such as effects of the solar wind pressure pulses, substorm explosions, etc.

9. References.

Boynton, R. J., M. A. Balikhin, S. A. Billings, H. L. Wei, and N. Ganushkina (2011), Using the NARMAX OLS-ERR algorithm to obtain the most influential coupling functions that affect the evolution of the magnetosphere, *J. Geophys. Res.,* 116, A05218, doi:10.1029/2010JA015505.

Lin, R. L., X. X. Zhang, S. Q. Liu, Y. L. Wang, and J. C. Gong (2010), A three-dimensional asymmetric magnetopause model, *J. Geophys. Res.,* 115, A04207, doi:10.1029/2009JA014235.

Newell, P. T., T. Sotirelis, K. Liou, C.-I. Meng, and F. J. Rich (2007), A nearly universal solar wind-magnetosphere coupling function inferred from 10 magnetospheric state variables, *J. Geophys. Res.,* 112, A01206, doi:10.1029/2006JA012015.

Tsyganenko, N. A. (2002), A model of the near magnetosphere with a dawn-dusk asymmetry 2. Parameterization and fitting to observations, *J. Geophys. Res.,* 107(A8), 1176, doi: 10.1029/2001JA000220.

Tsyganenko, N. A. (2009), Magnetic field and electric currents in the vicinity of polar cusps as inferred from Polar and Cluster data, *Ann. Geophys.*, 27, 1573–1582, 2009.

Tsyganenko, N. A. and C. T. Russell (1999), Magnetic signatures of the distant polar cusps: Observations by Polar and quantitative modeling, *J. Geophys. Res.,* 104(A11), 24,039–24,955.